Multiobjective Risk-Aware Path Planning in Uncertain Transient Currents: An Ensemble-Based Stochastic Optimization Approach

Sultan Albarakati, Ricardo M. Lima, Thomas Theußl, Ibrahim Hoteit, and Omar Knio

***Abstract*—A multiobjective, risk-aware framework is developed for optimal path planning of autonomous underwater vehicles operating in uncertain current. The uncertainty in the current is described in terms of a finite ensemble of flow realizations. A new optimization framework is proposed that accounts for the full variability of the ensemble in a single optimization problem whose solution may not necessarily coincide with any of the optimal deterministic paths corresponding to individual ensemble members. We formulate stochastic problems that aim to minimize a risk measure of the travel time or energy consumption, using a flexible methodology that enables the user to seamlessly explore various objectives, ranging from risk neutral to risk averse. We illustrate the application of the proposed approach using two case studies based on synthetic 2-D settings, and one case involving a real-world problem in the Gulf of Aden. The results are analyzed to assess the value of stochastic solution, guide the selection of suitable risk measures, and demonstrate the impact of the risk measures on the resulting path and on the distribution of travel times.**

***Index Terms*—Flow field ensemble, multiobjective optimization, Pareto front, path planning, risk-aware formulation.**

I. Introduction

AUTONOMOUS underwater vehicles (AUVs) are being employed for various applications, including collecting information on coastal ecosystems or underwater installations, search and rescue operations, inspection of intake and discharge of thermal plants, and management of shipping operations [1]–[3]. AUVs are also being utilized for military purposes, e.g., for surveillance of ocean vehicles, as well as in the mining, oil, and gas industries in the search for underwater resources [4]–[6].

AUVs normally navigate in strong and dynamic current environments. Thus, it is essential to conduct path planning so as to guarantee the efficiency and safeness of vehicles under such conditions. In addition, one is frequently faced with the problem of optimizing different objectives, such as total travel time, energy consumption, and quantity and quality of collected information [7]–[9], and possibly a combination of these at the same time. Another difficulty is the underlying uncertain character of predicted currents based on which the AUVs pathway planning is optimized. This is, nowadays, described by an ensemble of possible realizations of the ocean currents [10], [11], which needs to be taken into account in the planning.

While numerous studies have considered deterministic path planning problems, e.g., [6], [12], [12]–[22], path planning for AUVs operating in uncertain ocean environments has received less attention.

Pereira and Suhatme [23] and Pereira *et al.* [24] used Markov decision processes (MDP) to plan paths with minimum risk of collision between the vehicle and obstacles (static or dynamic) at the surface. Kularatne *et al.* [25] applied two methods to plan a path that minimizes the energy expenditure. The first method uses an MDP formulation to find an optimal cost policy, and the second uses a graph-based approach to compute a minimum expected cost path. Both methods consider a minimum energy cost function and try to minimize the expected cost of a path. Subramani *et al.* [26] and Subramani and Lermusiaux [27] applied stochastic level-set partial differential equations to find time optimal paths of vehicles navigating in uncertain flow fields. They find the path by first computing the distribution of exact time-optimal paths, obtained as the solutions of the stochastic dynamically orthogonal level set equations, and then determine the path that minimizes the risk of being suboptimal given the uncertain time-optimal path predictions. Wang *et al.* [28] used an ensemble approach to plan a path of AUVs in dynamic and uncertain ocean currents. The approach is based on generating a finite-size ensemble of the current field, and applying a Hamiltonian formalism to determine optimal paths corresponding to individual members of the ensemble. Individual solutions obtained for a particular realization are then evaluated against the remaining ensemble members, and probabilistic measures are then applied to select the best solution.

This work specifically focuses on ensemble-based approaches used for path planning in uncertain currents [26]–[28]. This is motivated by the fact that ensemble methods are now typically used to describe uncertainty in realistic ocean forecasts, and for the purpose of assimilating data ocean general circulation model (OGCM) simulations. Note that a common feature of previous

Manuscript received May 14, 2020; revised August 19, 2020 and February 2, 2021; accepted February 23, 2021. Date of publication April 30, 2021; date of current version October 13, 2021. This work was supported by research funding from the King Abdullah University of Science and Technology (KAUST) and used resources of the KAUST Core Labs. *(Corresponding author: Omar Knio.)*

Associate Editor: B. Englot.

The authors are with the King Abdullah University of Science and Technology, Thuwal 23955, Saudi Arabia (e-mail: sultan.albarakati@kaust.edu.sa; ricardo.lima@kaust.edu.sa; thomas.theussl@kaust.edu.sa; ibrahim.hoteit@kaust.edu.sa; omar.knio@kaust.edu.sa).

This article has supplementary downloadable material available at https://doi.org/10.1109/JOE.2021.3063196, provided by the authors.

Digital Object Identifier 10.1109/JOE.2021.3063196

ensemble-based approaches for AUV path planning under uncertainty [26]–[28] is that they relied on a simplified methodology, namely based on repeated applications of an essentially deterministic solver. Specifically, the simplification is based on optimizing the path based on individual realizations of the flow, evaluating the resulting deterministic solutions based on the other members of the ensemble, and then selecting the optimal path based on the probabilistic criterion or risk measure. This approach results in methods that are robust, but because they rely on an ensemble of paths determined for individual realizations of the current field, they may not result in an optimal solution.

The main contributions of this work are twofold: 1) new optimization models for path planning are developed that account for the full variability of the ensemble in a single optimization model; and 2) a multiobjective risk-aware path planning approach is introduced to minimize travel time and energy consumption in uncertain transient currents. A key feature of the proposed optimization models is that the solution may not necessarily coincide with any of the deterministic paths corresponding to individual ensemble members, which contrasts with the type of solutions obtained in [26]–[28]. To this end, we start by introducing a nonlinear deterministic 2-D path planning problem for steady and unsteady ocean current fields. Then, we extend it to a nonlinear stochastic programming problem to accommodate an uncertain flow field. We derive stochastic problems to minimize a risk measure of the travel time or energy consumption. We adopt an objective function that combines two risk measures: a risk-neutral and a risk-averse measure. The risk-neutral measure is defined by the expectation operator and the risk-averse measure by the Conditional Value at Risk (CVaR) [29]. We use the CVaR of the travel time and the CVaR of the energy consumption to measure the risk of long travel times and high energy consumptions, respectively. We calculate the value of stochastic solution (VSS) [30] to compare the stochastic solution against the deterministic solution. To estimate the value of perfect information, meaning the travel time reduction obtained with a perfect flow field forecast compared to the expected travel time calculated for an uncertain flow field, we calculate the expected value of perfect information (EVPI) [30]. To illustrate the application of the resulting framework, we consider two synthetic cases and a real-world case. The first case involves a steady stochastic current field, the second case involves an unsteady, stochastic double-gyre current field, and the third involves a path planning problem in the Gulf of Aden.

This article is organized as follows. Section II outlines the problem statement. Section III presents the stochastic optimization models for the minimum travel time and the minimum energy consumption. The scope of numerical experiments is defined in Section IV. Computational results are discussed and analyzed in Section V. Finally, we summarize our conclusions in Section VI.

II. Problem Statement

This work addresses the optimal path planning problem of an AUV based on a stochastic optimization formulation. We consider a 2-D uncertain flow field. The goal is to determine a path that is feasible for every realization of the flow field that minimizes a risk measure. The solution of this problem provides a sequence of waypoints from a fixed starting point to a fixed target.

In this setup, three types of objective functions are considered:

1) a risk measure of the travel time;
2) a risk measure of the energy consumption;
3) a risk measure of the energy consumption and travel time through a multiobjective minimization.

We propose a novel stochastic programming formulation based on a given ensemble of flow field forecasts. In this approach, the probability distribution of the flow field is discretized into scenarios, with each scenario corresponding to one member of the ensemble.

III. Stochastic Optimization Problems

We start by introducing the deterministic version of a 2-D trajectory planning problem before; then, we extend it to a stochastic programming problem to accommodate an uncertain flow field and minimize a risk measure of the travel time or energy consumption.

A. Deterministic Problem

The objective is to minimize the total travel time of a single AUV from starting point to destination, in the presence of current, and subject to kinematic constraints that limit the magnitude of the acceleration and velocity vectors. We consider the following 2-D trajectory optimization problem:

$$\min \int_{t_0}^{T} 1\, dt = T - t_0 \tag{1}$$

$$\text{s.t.} \frac{d\mathbf{x}(t)}{dt} = \mathbf{v}(t) + \mathbf{u}(\mathbf{x}(t), t) \tag{2}$$

$$\frac{d^2\mathbf{x}(t)}{dt^2} = \mathbf{a}(t) + \nabla \mathbf{u}(\mathbf{x}(t), t)\frac{d\mathbf{x}(t)}{dt} + \partial_t \mathbf{u}(\mathbf{x}(t), t) \tag{3}$$

$$\mathbf{x}(t_0) = \mathbf{x}_0 \tag{4}$$

$$\mathbf{x}(T) = \mathbf{x}^T \tag{5}$$

$$\sqrt{v_x^2(t) + v_y^2(t)} \leq v_{\max} \tag{6}$$

$$\sqrt{a_x^2(t) + a_y^2(t)} \leq a_{\max} \tag{7}$$

$$\mathbf{x}(t) \in \chi \subset \mathbb{R}^2 \tag{8}$$

$$\mathbf{v}(t), \mathbf{a}(t) \in \mathbb{R}^2 \tag{9}$$

$$T \in \mathbb{R} \tag{10}$$

where $\mathbf{x}(t) = (x(t), y(t))$ denotes the instantaneous position of the AUV at time t, $\mathbf{u}(\mathbf{x}(t), t) = (u_x(\mathbf{x}(t), t), u_y(\mathbf{x}(t), t)$ is the time varying current field, $\mathbf{v}(t) = (v_x(t), v_y(t))$ is the instantaneous velocity of the AUV with respect to the current, and $\mathbf{a}(t) = (a_x(t), a_y(t))$ is the acceleration of the vehicle with respect to the current. The total, ground-referenced, AUV velocity is $\mathbf{u} + \mathbf{v}$. The starting and ending time of the AUV trajectory are denoted by t_0 and T, respectively. In the stochastic programming problem, we extend these symbols to cover the

uncertain parameters and variables. Equations (2) and (3) are the kinematic constraints, (4) and (5) define the starting point and ending point, and (6) and (7) set upper bounds on the vehicle relative velocity and acceleration, respectively. The constraint in (8) forces the vehicle to navigate within the problem domain.

Note that in problem defined by (1)–(10), we do not consider a constraint for obstacles avoidance as proposed in [21]. In this work, we focus on extending this problem to a stochastic problem to cover uncertain flow fields. However, the stochastic version can be extended to include obstacle avoidance constraints.

B. Stochastic Programming Problems

We derive a stochastic programming problem based on the deterministic problem defined earlier and on 1) the discretization of the time a finite-difference time discretization using a second-order Taylor expansion; and 2) an ensemble-based discretization of the probability distribution function of the uncertain flow field. The optimal solution provides one path that is feasible for all the members of the considered ensemble.

Let $\mathcal{I} := \{0, 1, 2, 3, \ldots, I\}$ be a set with $I + 1$ grid points that form the basis of the time discretization, and $\mathcal{S} := \{1, 2, 3, \ldots, S\}$ be a set with S equiprobable scenarios that represent the discretization of the probability distribution function of the uncertain flow field. For each scenario $s \in \mathcal{S}$, we define an independent time grid discretization that shares the same grid points in $\mathcal{I}$. Therefore, for each grid point $i \in \mathcal{I}$, and for each scenario $s \in \mathcal{S}$, we have $t(i, s)$, $\Delta t(i, s)$, $\mathbf{v}(i, s)$, $\mathbf{a}(i, s)$, and $\mathbf{u}(\mathbf{x}(i), t(i), s)$, where $t(i, s)$ is the time for grid point i in scenario s, $\Delta t(i, s)$ is the time difference between $t(i, s)$ and $t(i - 1, s)$, $\mathbf{v}(i, s)$ and $\mathbf{a}(i, s)$ are the velocity and acceleration vectors at the grid point i in scenario s, respectively, and $\mathbf{u}(\mathbf{x}(i), t(i), s)$ is the flow field vector for scenario s in the position $x(i)$ and $t(i, s)$ at the grid point i.

In this setup, we assume that the AUV position vector $\mathbf{x}(i)$ is the same for each scenario, meaning $\mathbf{x}(i, s) = \mathbf{x}(i, s'),\ \forall s' \in \mathcal{S}$. Therefore, the proposed problems adopt a two-stage decision framework within each problem, where in the first-stage the path is determined, $\mathbf{x}(i)$, and in the second-stage, recourse actions ($\mathbf{v}(i, s)$, $\mathbf{a}(i, s)$) are used to adapt to the flow field realization and keep the AUV on the determined path. Note that the waypoints correspond to one sequence of positions, $\mathbf{x}(i)$, which are feasible for all scenarios of the flow field, and therefore, all scenarios share the same waypoints, but with a different timing.

1) Objective Function and Risk Measures: We adopt an objective function that combines two risk measures: 1) risk neutral; and 2) risk averse. The risk neutral is defined by the expectation operator and the risk averse by the CVaR [29]. We use the CVaR of the travel time and the CVaR of the energy consumption to measure the risk of long travel times and high energy consumptions, respectively. Basically, the CVaR operator is used to derive optimization solutions with paths that avoid the occurrence of long travel times or high energy consumptions for some realizations of the flow field.

The CVaR of a random variable is defined as the conditional expectation of the random variable to be greater than the value at risk of the random variable for the $1 - \alpha$ quantile (chosen by the user). We illustrate the concept of $\text{CVaR}_{1-\alpha}$ in Fig. 1. In the context of the present path planning problem, the $\text{CVaR}_{1-\alpha}$ of random travel time $T(\xi)$ is defined as

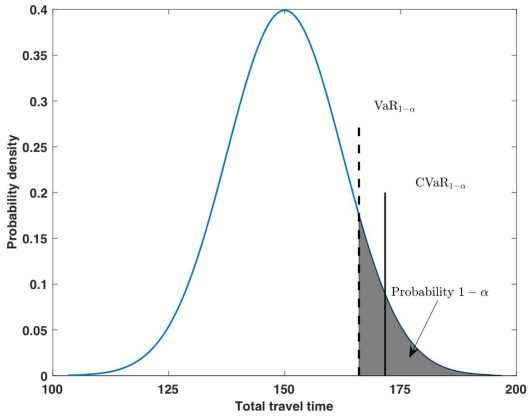

Fig. 1. Example of a final time distribution with $\text{VaR}_{1-\alpha}$ and $\text{CVaR}_{1-\alpha}$ marked as a dashed line and a continuous line, respectively.

$$\text{CVaR}_{1-\alpha}[T(\xi)] := \min_{\mu} \left\{ \mu + \frac{1}{1-\alpha} \mathbb{E}_{\xi}[C(\xi)] \right\} \tag{11}$$

where ξ is a random vector that parameterizes the stochastic variability of the current, μ denotes the value at risk, $\mathbb{E}_{\xi}$ is the mathematical expectation with respect to ξ, and $C(\xi)$ is a random variable defined as

$$C(\xi) := \min_{c(\xi)} \left\{ c(\xi) | c(\xi) \geq T(\xi) - \mu,\ c(\xi) \in \mathbb{R}^{+} \right\}. \tag{12}$$

Based on the definitions earlier and the discretization of the probability distribution function of the uncertain flow field, we consider two objective functions.

1) Minimization of a combination of risk measures of the travel time

$$\min_{\Delta} \{ \phi(\Delta, s) := \beta \mathbb{E}[T(s)] + (1 - \beta) \text{CVaR}_{1-\alpha}[T(s)] \}. \tag{13}$$

2) Minimization of a combination of risk measure of the energy consumption

$$\min_{\Delta} \{ \phi(\Delta, s) := \beta \mathbb{E}[E(s)] + (1 - \beta) \text{CVaR}_{1-\alpha}[E(s)] \}. \tag{14}$$

Here, $\Delta := (\mathbf{x}(i),\ \Delta t(i, s),\ \mathbf{v}(i, s),\ \mathbf{a}(i, s),\ \mu,\ c(s),\ T(s))$, $\beta \in [0,\ 1]$ is a parameter that defines the weight of the expectation and CVaR operators, $\mathbb{E}$ is the expectation with respect to the discrete distribution, and $E(\xi)$ is the energy consumption of the AUV.

C. Minimum Time Problem (MTP): Minimization of a Risk Measure of the Travel Time

We define the following formulation for the minimization of a combination of expected travel time and $\text{CVaR}_{1-\alpha}$ of the travel

time:

$$\text{MTP:} z^T := \min \quad \beta\left[\frac{1}{S}\sum_{s\in\mathcal{S}} T(s)\right] + (1-\beta) \times \left[\mu + \frac{1}{1-\alpha}\left(\frac{1}{S}\sum_{s\in\mathcal{S}} c(s)\right)\right] \tag{15}$$

$$\text{s.t.} \quad c(s) \geq T(s) - \mu \qquad \forall s \in \mathcal{S} \tag{16}$$

$$T(s) = \sum_{i\in\mathcal{I}} \Delta t(i,s) \qquad \forall s \in \mathcal{S} \tag{17}$$

$$t(i,s) = \sum_{ii\leq i\in\mathcal{I}} \Delta t(ii,s) \qquad \forall i \in \mathcal{I}, s \in \mathcal{S} \tag{18}$$

$$\mathbf{x}(i+1) = \mathbf{x}(i) + [\mathbf{v}(i,s) + \mathbf{u}(\mathbf{x}(i), t(i,s), s)]\,\Delta t(i,s) + \frac{1}{2}\mathbf{a}(i,s)\Delta t(i,s)^2 \qquad \forall i \in \mathcal{I},\ \forall s \in \mathcal{S} \tag{19}$$

$$\mathbf{v}(i+1,s) = \mathbf{v}(i,s) + \mathbf{a}(i,s)\Delta t(i,s) \quad \forall i \in \mathcal{I}, \forall s \in \mathcal{S} \tag{20}$$

$$\sqrt{v_x^2(i,s) + v_y^2(i,s)} \leq v_{\max} \qquad \forall i \in \mathcal{I}\ \forall s \in \mathcal{S} \tag{21}$$

$$\sqrt{a_x^2(i,s) + a_y^2(i,s)} \leq a_{\max} \qquad \forall i \in \mathcal{I}\ \forall s \in \mathcal{S} \tag{22}$$

$$\Delta t(i,s) \leq \Delta t_{\max} \qquad \forall i \in \mathcal{I}, \forall s \in \mathcal{S} \tag{23}$$

$$\mathbf{x}(0) = \mathbf{x}_0 \tag{24}$$

$$\mathbf{x}(N) = \mathbf{x}^T \tag{25}$$

$$\mathbf{x}(i) \in \chi \subset \mathbb{R}^2 \quad \forall i \in \mathcal{I} \tag{26}$$

$$\mathbf{v}(i,s),\ \mathbf{a}(i,s) \in \mathbb{R}^2 \qquad \forall i \in \mathcal{I}, \forall s \in \mathcal{S} \tag{27}$$

$$c(s) \in \mathbb{R}^+ \qquad \forall s \in \mathcal{S} \tag{28}$$

$$t(i,s),\ \Delta t(i,s) \in \mathbb{R}^+ \qquad \forall i \in \mathcal{I}, \forall s \in \mathcal{S} \tag{29}$$

$$\mu \in \mathbb{R}^+ \tag{30}$$

$$T(s) \in \mathbb{R}^+ \qquad \forall s \in \mathcal{S}. \tag{31}$$

We denote this problem by MTP. It is a nonlinear stochastic programming problem with bilinear and quadratic terms. The objective function corresponds to the function defined in (13). The first term is the expectation and the second the CVaR with respect to the discrete distribution of the travel times, where S denotes the number of discrete equiprobable scenarios, and β and α are fixed parameters. Equation (17) defines the total travel time for each scenario s as the summation of $\Delta t(i,s)$ over all grid points, (18) defines the time for grid point i in each scenario s. Equation (16) results from the definition of CVaR using the optimization formulation in (11) and (12). Equations (19)–(22) are the discrete version of the kinematic equations and bounds on the relative velocity and acceleration. The step size is bounded by $\Delta t_{\max}$ in (23).

The problem formulation is based on a sequence of waypoints with position $x(i)$, which are common to all scenarios, but in each scenario each waypoint has a distinct timing evaluated using (18).

D. Minimum Energy Problem (MEP): Minimization of a Risk Measure of the Energy Consumption

The path planning problem to minimize a combination of the expectation and CVaR of the energy consumption is formulated for a fixed travel time. The solution of this problem provides also a path that is feasible for each scenario of the flow field ensemble. The problem definition is

$$\text{MEP:} z^E := \min \beta\left[\frac{1}{S}\sum_{s\in\mathcal{S}} E(s)\right] + (1-\beta)\left[\mu + \frac{1}{1-\alpha}\left(\frac{1}{S}\sum_{s\in\mathcal{S}} c(s)\right)\right] \tag{32}$$

$$\text{s.t. } T^{\text{fixed}} = \sum_{i\in\mathcal{I}} \Delta t(i,s) \qquad \forall s \in \mathcal{S} \tag{33}$$

$$E(s) = \sum_{i\in\mathcal{I}} \left(||\mathbf{v}(i,s)||_2^2 \cdot \Delta t(i,s)\right) \qquad \forall s \in \mathcal{S} \tag{34}$$

$$c(s) \geq E(s) - \mu \qquad \forall s \in \mathcal{S} \tag{35}$$

$$(18) \text{ to } (30) \tag{36}$$

$$E(s) \in \mathbb{R}^+ \qquad \forall s \in \mathcal{S}. \tag{37}$$

In the MEP, the objective function refers to energy consumption and it corresponds to the function defined in (14). The two terms and parameters S, β, and α are defined as in the MTP. In (33), we fix the total travel time for each scenario. Equation (34) is the total energy consumption for each scenario s. Equation (35) results from the definition of CVaR using the optimization formulation in (11) and (12).

E. Multiobjective Minimization of a Risk Measure of the Energy Consumption and Travel Time

The two problems formulated earlier are also integrated into a multiobjective framework. We adopt the ϵ-constraint method [31] in a framework where for a fixed travel time, we minimize the energy consumption using the MEP. With the solution pair (time, energy), we build a Pareto-optimal solution curve.

F. Solution Approach

Our solution approach starts by choosing values for the risk parameters β and α, setting the time horizon T_h over which the MEP is solved, and the number of steps $k_{\max}$ used to discretize this time horizon. An initialization of the MTP is, then, determined by solving the deterministic problem for a single, randomly-selected, ensemble member. With this initialization, we solve the MTP for the entire ensemble, yielding the minimum of a risk measure of the travel time. This solution is, then, used to initialize the first MEP, with fixed travel time equal to T_m, where $T_m = \mathbb{E}[T(s)]$ is the expected travel time of the MTP solution. Note that T_h must be greater than T_m. The MEP problems for

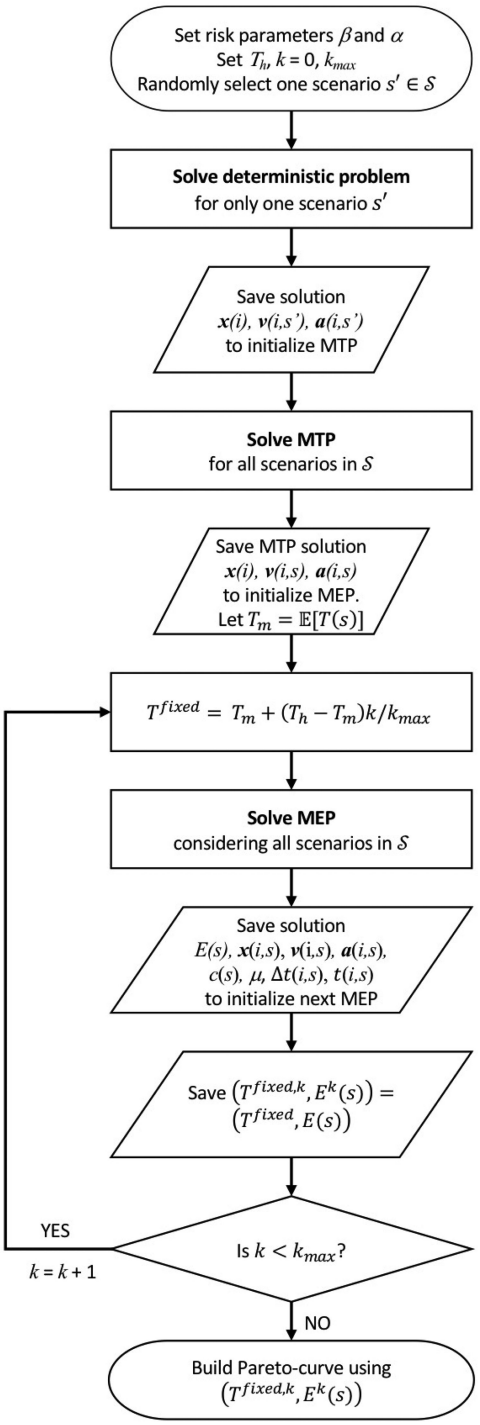

Fig. 2. Flowchart of the solution approach.

$k = 1, \ldots, k_{\max}$, are solved in a similar fashion, i.e., using the solution of the previous MEP as initialization and a fixed travel time of $T_m + (T_h - T_m)k/k_{\max}$. The Pareto curve is built by combining the results of the MTP and the $k_{\max}$ MEP problems between T_m and T_h. See Fig. 2 for details.

G. Feasibility of Solutions

The solution algorithm yields one path that is feasible for each member (scenario) of the flow field ensemble. In general, if at least for one scenario the current is stronger than the maximum AUV velocity, then the problem may become infeasible. However, because the flow field varies with the position solutions may still be obtained that take advantage of the current variability to reach the target. For example, in the results presented in Section V-A, there are paths that initially move away from the target but later adapt toward the target. In [21] and [32], it is shown that in 3-D deterministic settings, optimal solutions can be determined that take advantage of the surface currents, as well as by changing depth along the path. As an alternative, the model can be extended to include slack variables for the bounds on the velocity and acceleration, with a large penalty value in the objective function for nonzero positive slack variables. Such approach can provide solutions in cases where the AUV may not avoid strong unfavorable currents.

H. Evaluation of Deterministic and Stochastic Solutions

We compare the stochastic and deterministic solutions using a measure known as the VSS [30]. The VSS provides a measure of the expected loss when using the deterministic solution. In addition, we calculate the EVPI [30] that provides an indication of the value of perfect flow field forecasts. For the case studies addressed, with $\beta = 1$, the loss and value are measured in terms of travel time or energy consumption. Before presenting the expressions for the VSS and EVPI, we introduce the following nomenclature and notation.

1) The optimal solution of MTP or MEP as SP $:= z^T$ or SP $:= z^E$.
2) The expected value (EV) problem, defined by using the average flow field as a single scenario in the MTP or MEP.
3) The EV solution $\overline{\mathbf{x}}(i)|_{\overline{u}}$ obtained from the EV problem.
4) The expected result of the EV solution EEV $:= \mathbb{E}[\min \phi(\overline{\mathbf{x}}(i)|_{\overline{u}}, s)]$. EEV is the average value of the objective functions obtained from the MTP or MEP with $\overline{\mathbf{x}}(i)|_{\overline{u}}$ fixed and one member of the flow field ensemble per problem.
5) $\Delta^*|_s$ denoting the solution of the MTP or MEP considering only one scenario s, i.e., one element of the ensemble per problem.
6) The EV of the optimal solution, also known as wait-and-see solution, as WS $:= \mathbb{E}[z^T(\Delta^*|_s)]$ or WS $:= \mathbb{E}[z^E(\Delta^*|_s)]$ for the MTP and MEP, respectively.

Based on the aforementioned notation and definitions, we define the VSS and EVPI as

$$\text{VSS} := \text{EEV} - \text{SP} \tag{38}$$

$$\text{EVPI} := \text{SP} - \text{WS}. \tag{39}$$

IV. Numerical Experiments

To illustrate the results of the proposed AUVs pathway optimization models, we consider two synthetic cases and a realistic case. The first case involves a steady stochastic current, which we refer to as Case 1. The second case, Case 2, involves a stochastic unsteady double-gyre flow. The third case, Case 3, considers an unsteady OGCM ensemble.

TABLE I
DOMAIN SIZE AND PARAMETERS FOR CASES 1 AND 2

Parameters	Values			
	Case 1		Case 2	
	MTP	MEP	MTP	MEP
$(x_{\min}, y_{\min})$	$(0,0)$			
$(x_{\max}, y_{\max})$	$(100,50)$			
$\mathbf{x}_0 = (x_0, y_0)$	$(5,50)$		$(5,45)$	
$\mathbf{x}^f = (x^f, y^f)$	$(95,50)$		$(95,5)$	
$D_{\mathbf{x}_0 \to \mathbf{x}^f}$	90		98.5	
$v_{\max}$	1	1	1.5	1.5
$a_{\max}$	1	1	1.5	1.5
$\Delta t_{\max}$	1.5	1.5	1	1.5
I	180	180	130	180
S	50	50	48	48
α	0.90	0.90	0.90	0.90

TABLE II
DOMAIN SIZE AND PARAMETERS FOR CASE 3

Parameters			Values	Units
Case 3	Domain χ	$(x_{\min}, y_{\min})$	$(1466090, 117500)$	m
		$(x_{\max}, y_{\max})$	$(1766880, 248750)$	m
		$D_{\mathbf{x}_0 \to \mathbf{x}^f}$	234931.3	m
		$\Delta t_{\max}$	3600	s
		$v_{\max}$	1.5	m/s
		$a_{\max}$	1.5	m/s^2
		$u_{\max}$	2	m/s
		$T_{\max}$	60	h
		I	60	
		S	32	
		α	0.90	
	Instance I	$\mathbf{x}_0$	$(1728207, 213518)$	m
		$\mathbf{x}^f$	$(1499340, 160484)$	m
	Instance II	$\mathbf{x}_0$	$(1499340, 160484)$	m
		$\mathbf{x}^f$	$(1728207, 213518)$	m

The parameters defining the vehicle, domain, and models used in Cases 1 and 2 are outlined in Table I. For Case 3, we consider two instances, as defined in Table II.

A. Case 1

Case 1 considers a steady stochastic current defined by

$$u_x(\mathbf{x}, \xi) = 0.8 \cdot \exp(-(y-50))^2 \cdot \cos\left(\frac{2\pi \cdot x}{40} + \pi\eta(\xi)\right)$$
$$u_y(\mathbf{x}, \xi) = 0.0 \tag{40}$$

where $\eta(\xi)$ is a random variable that defines the uncertainty in the horizontal direction. We adopt a discrete distribution for $\eta(\xi)$, where $\eta(\xi) = i/S,\ i = 1, \ldots, S$. Fig. 3 depicts four realizations of the uncertain flow field; the horizontal current magnitude $u_x(\mathbf{x}, s)$ is color coded in the background. Note that the maximum horizontal current magnitude is 0.8.

B. Case 2

We consider a more complex current field, consisting of a stochastic unsteady double-gyre [33]. Specifically, the uncertain current field is expressed as

$$u_x(\mathbf{x}, t, \xi) = -\pi(\gamma + A(\xi))\sin(\pi f(x, \xi))\cos(\pi y)$$
$$u_y(\mathbf{x}, t, \xi) = -\pi(\gamma + A(\xi))\cos(\pi f(x, \xi))\sin(\pi y)\frac{\mathrm{d}f(x, \xi)}{\mathrm{d}x} \tag{41}$$

where

$$f(x, \xi) = a(t, \xi) \cdot x^2 + b(t, \xi) \cdot x$$
$$a(t, \xi) = (\delta + \epsilon(\xi))\sin(\omega \cdot t)$$
$$b(t, \xi) = 1 - 2(\delta + \epsilon(\xi))\sin(\omega \cdot t).$$

The parameters γ, δ, and ω are assumed fixed; we set $\gamma = 0.1, \delta = 0.2, \omega = \pi/40$. The random variables $A(\xi)$ and $\epsilon(\xi)$ are assumed to be independent and uniformly distributed over the intervals [0,0.1], and [0, 0.2], respectively. Using these parameters, we generate 48 time-dependent current field scenarios, which are illustrated in Fig. 4. In this figure, each scenario is represented by one arrow at every location depicted. Note that the maximum current magnitude is 0.6.

C. Case 3

In this case, we consider an ensemble of time-dependent ocean fields simulated using an assimilative OGCM of the Red Sea, which was developed in [34] and [35] and exploited in [32] for optimal path planning in a deterministic current setting. We provide a brief description of the system, which is largely adapted from that provided in [32].

The underlying assimilation system operates sequentially as cycles of forecast-analysis steps, using the MIT OGCM (MIT-gcm) for forecasting the Red Sea circulation, and an ensemble Kalman filter (EnKF) for updating the model forecasts with satellite sea surface height and temperature observations every time they become available [36]. The system domain extends from 30°E to 50°E and from 10°N to 30°N, covering the whole Red Sea, the Gulf of Suez, the Gulf of Aqaba, and the Gulf of Aden. To measure Euclidean distance in the problem domain, we consider 30° longitude, 10° latitude, and the sea level as the origin, and measure all the distances from this point. The system was configured on a spherical grid with a $0.04^\circ \times 0.04^\circ$ horizontal resolution, resulting in 500×500 grid points, and 50 vertical layers ranging from 4 m at the surface to 300 m near the bottom. After validating the model outputs with available *in situ* and satellite remote sensing observations [37], [38]; this ensemble assimilation system was integrated to generate flow-fields conditioned for the month of January 2006.

From this data set, we selected 32 ensemble members at specific times, forming regular 3-day-long intervals. Once the nodal velocities are defined, the velocity vector at arbitrary spatial locations is determined through a tricubic interpolation method as described in [21]. Finally, the local velocity values are interpolated linearly between neighboring time snapshots to describe the time-dependent velocity vector.

We consider a time-dependent ensemble current field, given by an OGCM simulation of the oceanic circulation in the Gulf of Aden. Fig. 5 shows an overview of the surface current field

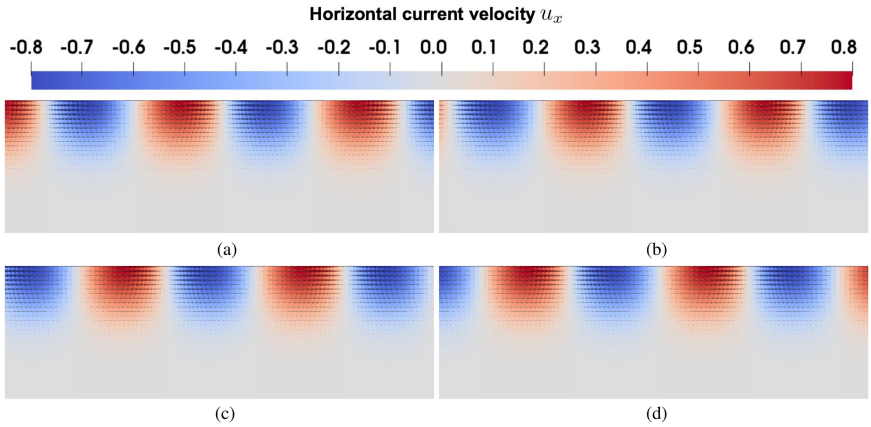

Fig. 3. Current field for four different scenarios of Case 1. u_x is the horizontal current velocity. (a) Scenario 1. (b) Scenario 16. (c) Scenario 32. (d) Scenario 50.

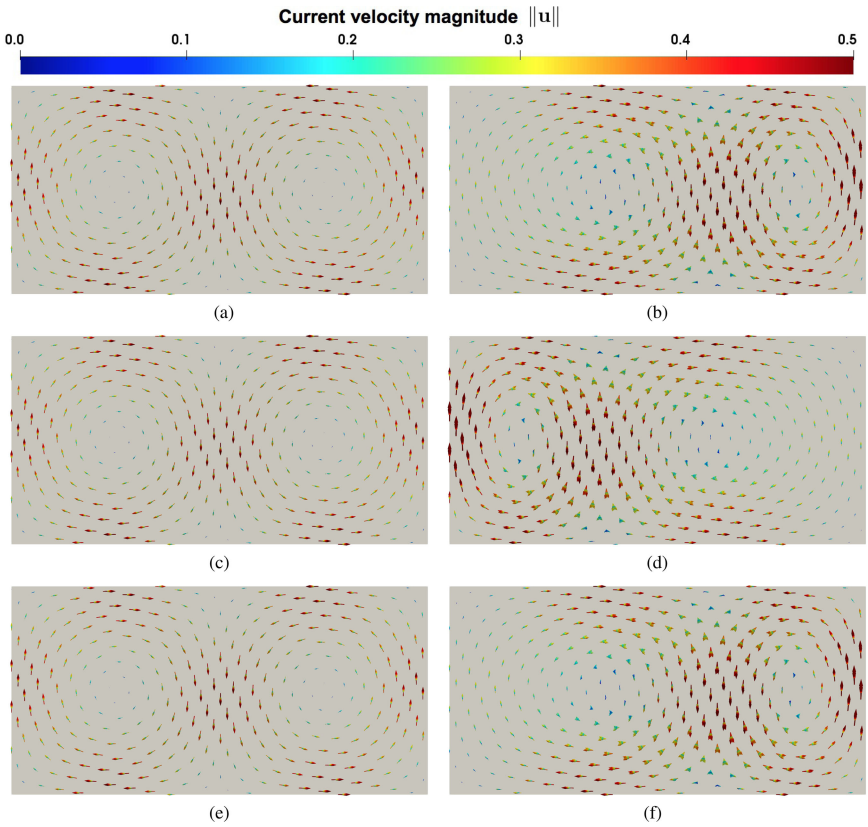

Fig. 4. Current field of Case 2 with snapshots at six different times. To visualize uncertainty in the current field, multiple arrows are plotted at each grid point that corresponds to different realizations of the local velocity vector. (a) Snapshot at time 0. (b) Snapshot at time 20. (c) Snapshot at time 40. (d) Snapshot at time 60. (e) Snapshot at time 80. (f) Snapshot at time 100.

in the Gulf of Aden, for six time snapshots of the 32 ensemble members. To illustrate the variability of the flow, the velocity vector in each member is represented by one arrow at each location depicted.

As further discussed below, in Case 3, we consider two instances. In Instance I, the AUV starts at point A and its destination is point B; see Fig. 5(a). In Instance II, the start point is B and the destination is at point A.

V. Results

We implemented the proposed approach using the software system general algebraic modeling system (GAMS) [39]. The cases were optimized using the open-source software package for large-scale nonlinear optimization IPOPT 3.12 [40]. The runs were performed on a workstation with 2.5-GHz CPUs and 128-GB RAM. In Cases 1–3, it took 16 min to solve MTP, and approximately 2 min to solve MEP for each fixed travel time.

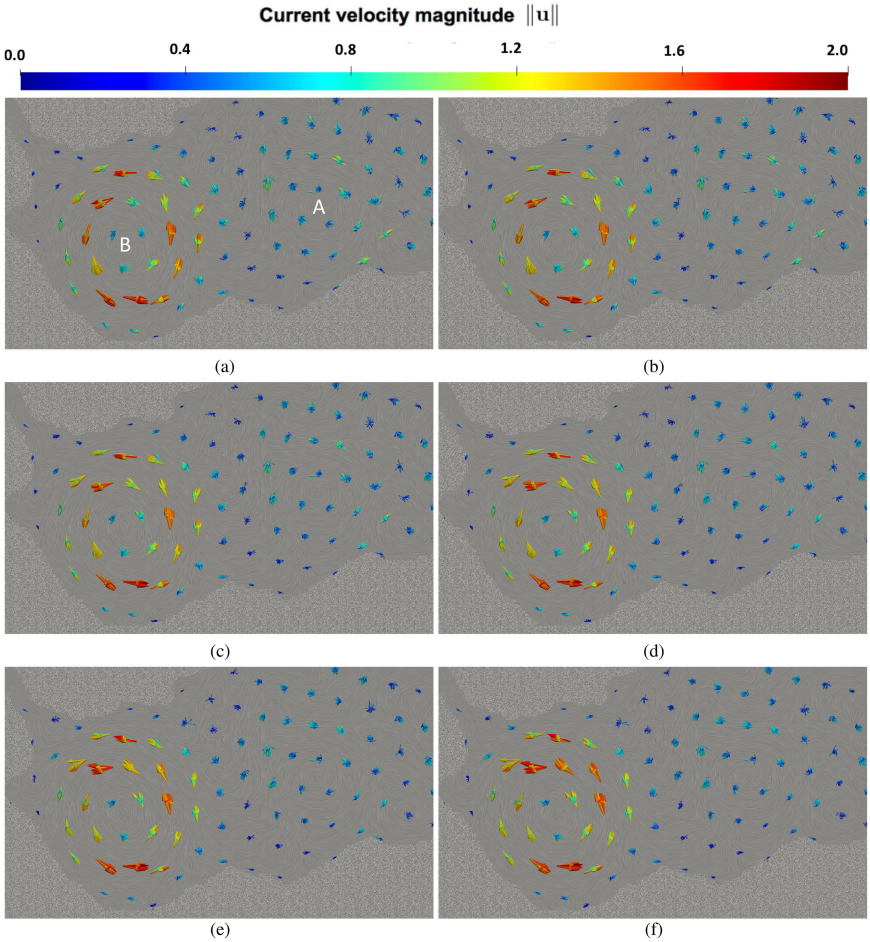

Fig. 5. Current field of Case 3 with snapshots at six different times. The uncertainty in the current field is represented by multiple arrows plotted at each grid point that corresponds to different realizations of the local velocity vector. (a) Snapshot at time 6 h. (b) Snapshot at time 12 h. (c) Snapshot at time 18 h. (d) Snapshot at time 24 h. (e) Snapshot at time 30 h. (f) Snapshot at time 36 h.

The size of the MTP is 54 514 variables and 63 052 equations in Case 1, 75 338 variables and 81 219 equations in Case 2, and 19 546 variables and 19 267 equations in Case 3. In this section, we present the results of the stochastic optimization experiments for the case studies described earlier. For each case, we present the following results.

1) The optimal solution paths: a) path for the optimal solution of MTP or MEP; b) path for the EV solution, $\overline{\mathbf{x}}(i)|_{\overline{u}}$; and c) path obtained from solving the MTP or MEP for each element of the ensemble.
2) Distributions of the positions as a function of the scenarios. For each path, we use spheres to show the distribution of positions along the path, one position per scenario, at specific times. Green spheres are used for $\beta = 1$, yellow spheres for $\beta = 0$, a red sphere for the EV solution, and blue spheres for the distribution of positions obtained from the MTP or MEP for each element of the ensemble with the path from the EV solution fixed.
3) Risk management results showing the expected travel time and CVaR of the travel time as a function of β for the MTP.
4) Assessment of the stochastic solutions using the VSS and EVPI as a function of β for the MTP.
5) Distributions of times as a function of scenarios using box-plots with the distribution of the time for each scenario for each grid point obtained with the MTP for $\beta = 0$, $\beta = 1$, the EV solution, and the solution of the MTP for each element of the ensemble with the path from the EV solution fixed.
6) Pareto-optimal curves for time–energy, including box plots depicting the distribution of energy consumption for each travel time, for both $\beta = 0$ and $\beta = 1$.

Animations of the AUV paths and the ocean current for the MTP and MEP for both cases are provided in the supplementary material.

A. Case 1

A stochastic synthetic field is considered here with a composite of vertical shear and cosine function as given by (40).

Fig. 6 shows that the optimal path obtained with the EV solution is significantly different from the optimal paths obtained with the MTP with $\beta = 0$ or $\beta = 1$. This is a relevant result because it highlights the difference in the paths between the deterministic solution (obtained with the average current)

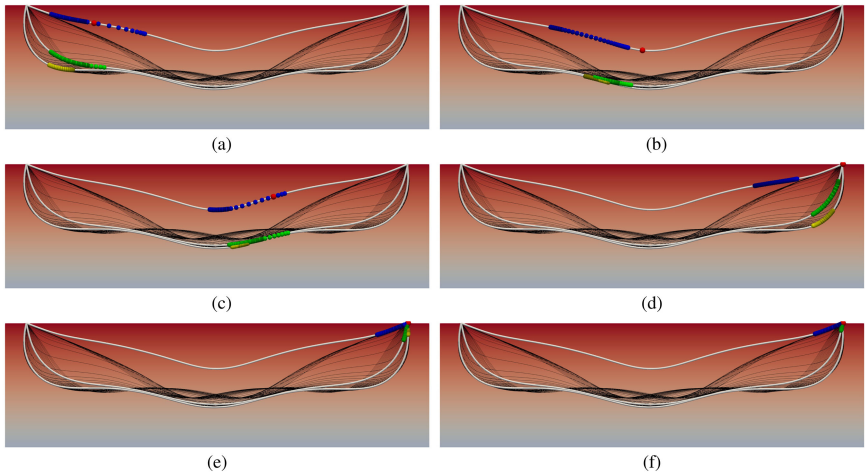

Fig. 6. Case 1. Optimal paths (lines) and distributions of the AUV position (spheres) at selected times, obtained from the solutions of the MTP. The green spheres (●) indicate the solution with $\beta = 1$ (risk neutral), the yellow spheres (●) the solution with $\beta = 0$ (risk averse), the red sphere (●) is the expected current solution, and the blue spheres (●) the solution of the MTP for each element of the ensemble with the path (from the mean current solution) fixed. Thin black lines indicate the (deterministic) solutions of the MTP considering only individual elements of the ensemble. Background color gradient indicates depth. (a) Snapshot at time 25. (b) Snapshot at time 50. (c) Snapshot at time 70. (d) Snapshot at time 108. (e) Snapshot at time 124. (f) Snapshot at time 127.

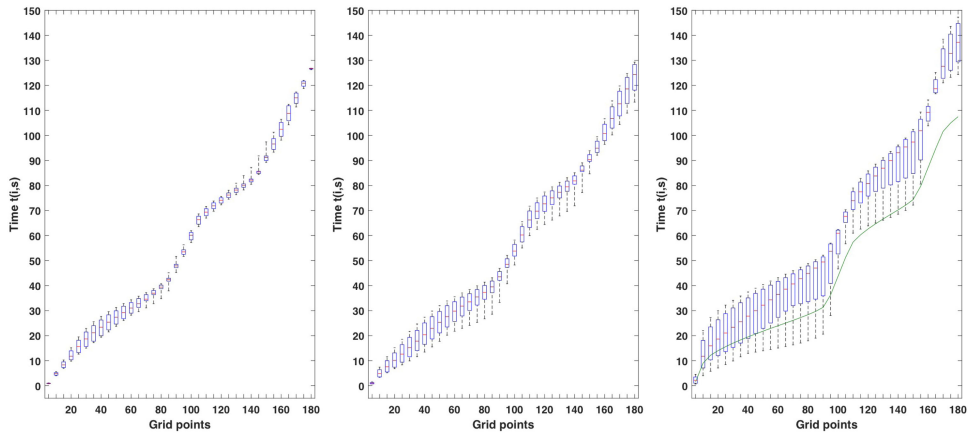

Fig. 7. Case 1. Box-plot of the distribution of times $t(i, s)\ \forall s \in \mathcal{S}$, for selected grid points i, obtained from the solution of the MTP. In (c), the green line is the mean current solution and the boxes depict the distribution of times for each element of the ensemble with the path (from the mean current solution) fixed. In each box, the central red mark indicates the median, and the bottom and top edges of the box indicate the 25th and 75th percentiles of the travel time distribution, respectively. (a) $\beta = 0$ (risk averse). (b) $\beta = 1$ (risk neutral). (c) Expected value solution.

and the stochastic solution. This figure also reveals that the stochastic solution is not contained in the individual solutions obtained from the MTP with individual elements of the ensemble.

The subfigures in Fig. 6 at different snapshot times show that the risk-neutral solutions ($\beta = 1$) have a wider distribution of positions than the risk averse ($\beta = 0$). In most of the snapshot times, the distribution of positions of the individual solutions obtained from the MTP with individual elements of the ensemble is also the widest. Fig. 7 provides additional results, where it is shown that the EV solution leads to a wider distribution of times in the individual solutions obtained from the MTP with individual elements of the ensemble, and that the solution with $\beta = 0$ results in the narrowest distribution of times.

Fig. 6 also shows that the EV solution has the minimum expected travel time. This result is probably due to averaging the current that has a substantial smoothing effect, due to the current setup where the current alternates between going left and right.

Fig. 8 shows that the expected travel time decreases as β increases, whereas the CVaR of the travel time increases as β increases. This figure provides a guide to choose a suitable β that represents a tradeoff between the increment of the expected travel time and reduction of the CVAR of the travel time, compared to the solution for $\beta = 1$.

The value of the stochastic solution is demonstrated by three results: 1) the difference between the path of the EV solution and the path from the MTP; 2) the distribution of the travel

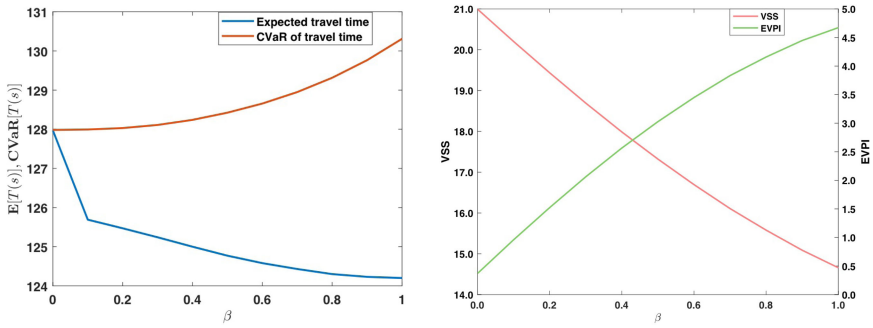

Fig. 8. Case 1. Left: Expected travel time and CVaR of the travel time as a function of the risk parameter β from the MTP solution. Right: VSS and EVPI versus β for the MTP.

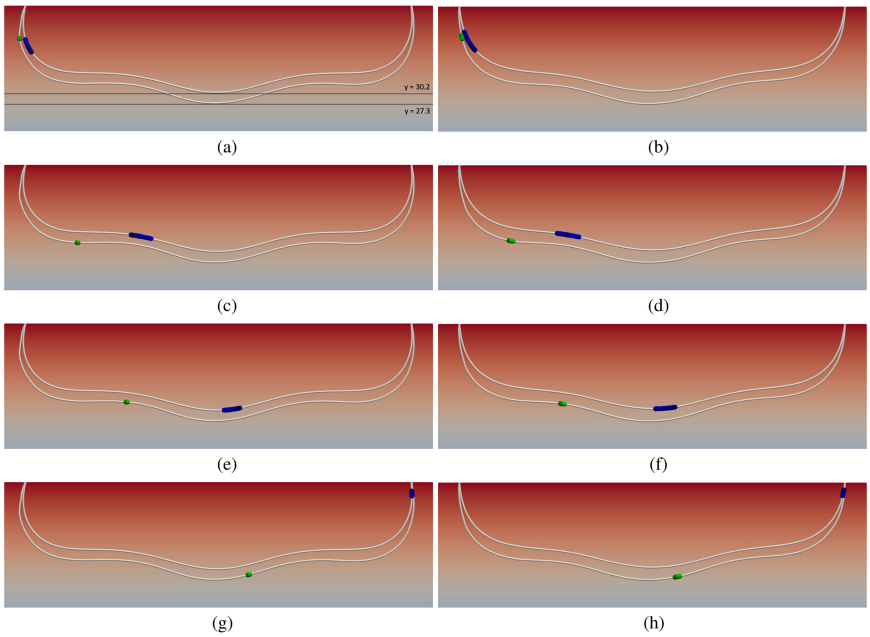

Fig. 9. Case 1. Optimal paths (lines) and distributions of the position (spheres) of the AUV at given time snapshots, obtained from the solutions of the MEP. The green spheres (●) indicate the solution with $T^{\text{fixed}} = 235$, and the blue spheres (●) with $T^{\text{fixed}} = 136$. Background color gradient indicates depth. (a) β= 0 (risk averse), snapshot at time 12. (b) β= 0 (risk neutral), snapshot at time 12. (c) $\beta = 0$ (risk averse), snapshot at time 45. (d) $\beta = 0$ (risk neutral), snapshot at time 45. (e) $\beta = 0$ (risk averse), snapshot at time 72. (f) $\beta = 0$ (risk neutral), snapshot at time 72. (g) $\beta = 0$ (risk averse), snapshot at time 132. (h) $\beta = 0$ (risk neutral), snapshot at time 132.

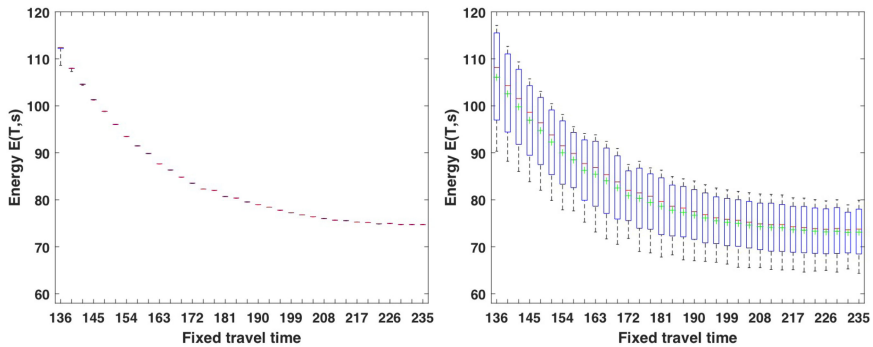

Fig. 10. Case 1. Time–energy Pareto-optimal curve with box-plot for the distribution of $E(s)\,\forall s \in \mathcal{S}$. In each box, the central red mark indicates the median, the green (+) indicates the mean, and the bottom and top edges of the box indicate the 25th and 75th percentiles of the distribution of energy spent, respectively. (a) $\beta = 0$ (risk averse). (b) $\beta = 1$ (risk neutral).

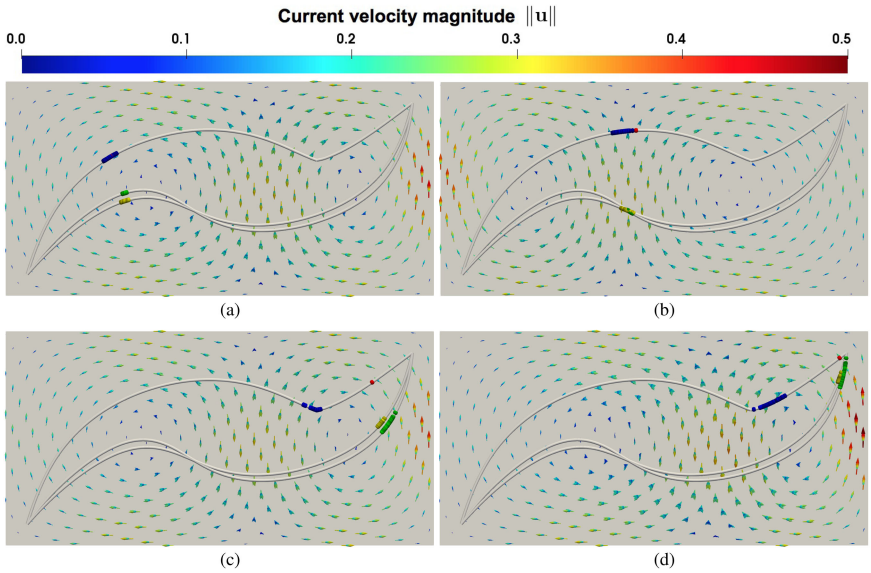

Fig. 11. Case 2. Optimal paths (lines), distributions of the AUV position (spheres) at selected times, obtained from the solutions of the MTP. The arrows represent the local velocity vectors of the flow field ensemble. The green spheres (●) indicate the solution with $\beta = 1$ (risk neutral), the yellow spheres (●) the solution with $\beta = 0$ (risk averse), the red sphere (●) is the mean current solution, and the blue spheres (●) the solution of the MTP for each element of the ensemble with the path (from the mean current solution) fixed. (a) Snapshot at time 20. (b) Snapshot at time 47. (c) Snapshot at time 88. (d) Snapshot at time 98.

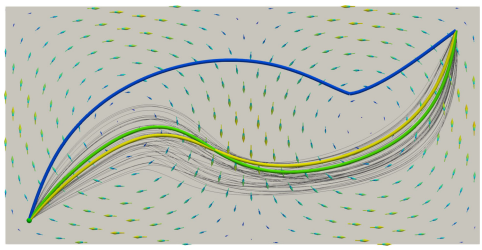

Fig. 12. Case 2. Optimal paths obtained from the solution of the MTP. The arrows represent the local velocity vectors of the flow field ensemble. The green path is obtained with $\beta = 1$ (risk neutral), the yellow path with $\beta = 0$ (risk averse), and the blue path is the expected current solution. Thin black lines indicate the (deterministic) solutions of the MTP considering only individual elements of the ensemble.

times obtained from the three approaches: a) the MTP, b) the EV solution, and c) from using the MTP for each element of the ensemble with the path from the EV solution fixed; and 3) the positive values of VSS. The VSS and EVPI for the MTP are given in Fig. 8, where one can see that the VSS increases as we seek more risk-averse solutions (decreasing β), whereas the EVPI increases with β.

In the case of the MEP, we study the energy consumption of the vehicle for fixed travel times, ranging from $T^{\text{fixed}} = 136$ to $T^{\text{fixed}} = 235$. The paths for $T^{\text{fixed}} = 136$ and $T^{\text{fixed}} = 235$ for $\beta = 0$, $\beta = 1$ are shown in Fig. 9.

We observe that for the larger travel time, the vehicle seeks regions of uniform near-zero velocity current, which correspond to lower depths, so that it can reduce the relative velocity and energy consumption without being affected by the current velocity; see Fig. 9. Therefore, for the larger travel time, the vehicle is less affected by the distribution of the currents, as can be observed by the narrow distribution of the green spheres in Fig. 9. In contrast, for the shortest travel time, the vehicle navigates closer to the surface, where the current variability has higher impact on the distribution of positions.

Fig. 10(a) and (b) illustrates the time–energy Pareto curves with box-plots for $\beta = 0$ and $\beta = 1$, respectively. The energy consumption decreases monotonically with increasing the travel time, for both values of β.

First, analyzing the case $\beta = 1$, one observes that the distributions of the energy consumption become narrow as the (selected) travel time increases. This effect is explained by noticing that increasing the travel time, the path is driven to lower regions, and thus, the impact of the current variability on the energy consumption is smaller. However, given that the regions near the starting and ending points still have appreciable and highly varying currents, the distribution of energy consumption does not collapse to a narrow distribution.

The box-plot for $\beta = 0$ shows that the distributions of the energy consumption almost collapsed to a single value. Compared to $\beta = 1$, with $\beta = 0$, more robust results are obtained, in the sense that the optimal path does not lead to variations of the energy consumption as observed in Fig. 10(b).

B. Case 2

In this case, we consider a stochastic unsteady double-gyre flow. Fig. 11 shows that the path obtained with the EV solution differs substantially from the path of the stochastic solutions obtained with the MTP for $\beta = 0$ and $\beta = 1$. However, the paths obtained with the MTP are quite similar. This figure provides also a dynamic view of the distribution of the positions, given by

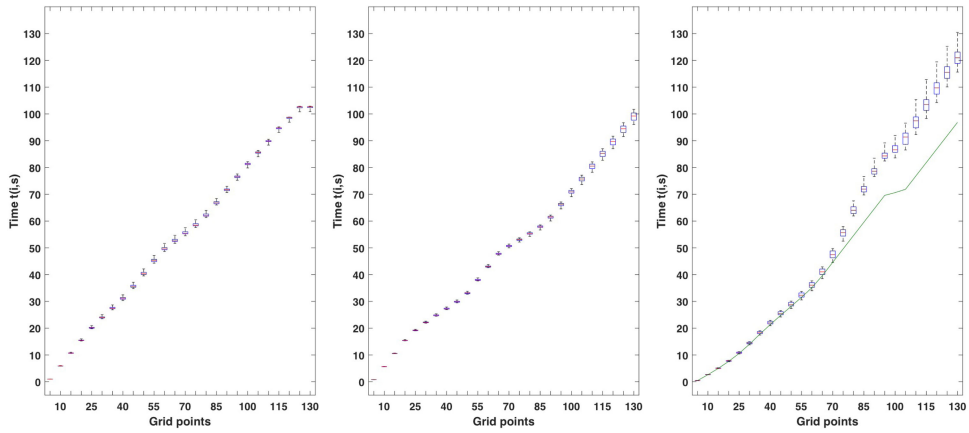

Fig. 13. Case 2. Box-plot of the distribution of times $t(i,s)$, $\forall s \in \mathcal{S}$, for selected grid points i, obtained from the solution of the MTP. In (c), the green line is the EV solution and the boxes correspond to the solution of the MTP for each element of the ensemble with the path (from the EV solution) fixed. In each box, the central red mark indicates the median, and the bottom and top edges of the box indicate the 25th and 75th percentiles of the travel time distribution, respectively. (a) $\beta = 0$ (risk averse). (b) $\beta = 1$ (risk neutral). (c) Expected value solution.

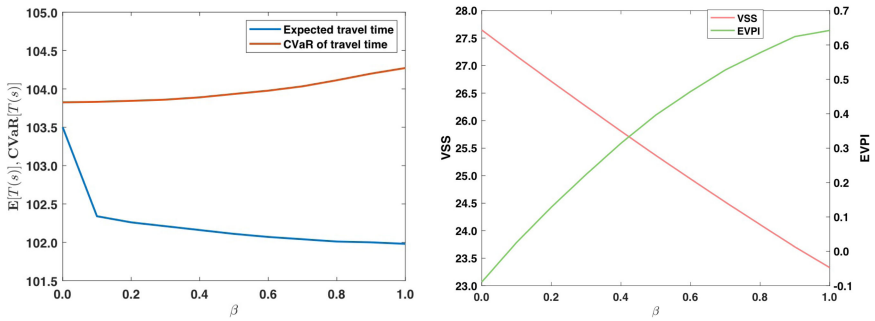

Fig. 14. Case 2. Left: Expected travel time and CVaR of the travel time as a function of the risk parameter β from the MTP solution. Right: VSS and EVPI versus β for the MTP.

the colored spheres, for each path. The solution from the MTP with $\beta = 0$ has the narrowest distribution of positions, whereas the distributions of the two other solutions change with time. Also, for times $t > 47$, the red sphere representing the EV solution detaches from the distribution of particles corresponding to individual members of the ensemble along the path of the EV solution.

Fig. 12 simultaneously depicts the individual optimal paths corresponding to an individual element of the ensemble. These (deterministic) paths have a similar trend to the paths obtained with the MTP, but there is a wide range between them, which makes it difficult to select one of them as the optimal solution under uncertainty.

Fig. 13 outlines that both solutions with $\beta = 0$ and $\beta = 1$ have a narrow distribution of the times at specific grid points until approximately grid point 90. Afterward, the distribution of the times increases, but still, it remains narrower than the distribution of the times obtained along the path from the EV solution.

Fig. 14 shows a steep decrease in the expected travel time solution from $\beta = 0$ to $\beta = 0.1$, whereas for $\beta > 0.1$, it has a small variation. The CVaR of the travel time increases with β but without a significant change.

The trends of the VSS and EVPI as a function of β are similar to the ones of Case 1. Again, the VSS is higher for risk-averse solutions, indicating that these solutions are more distant from the deterministic solution than the risk-neutral solution. This is explained by the fact that the deterministic solution is based on the average flow field.

The value of the stochastic solutions is clearly captured in Fig. 11(d), which highlights the difference between the stochastic solutions, green, yellow, and blue spheres. Note that the red sphere indicates the solution obtained with an average current, which is then evaluated using the individual members of the flow ensemble and visualized using the blue spheres, which all arrive later than the yellow and green spheres. The difference in travel times is well illustrated by the distribution of the times in Fig. 13(c), which shows that the blue spheres arrive later than the green and yellow spheres; see the final boxes in Fig. 13(a) and (b).

Using the MEP, we study the energy consumption for fixed travel times, from $T^{\text{fixed}} = 80$ to $T^{\text{fixed}} = 170$. The paths

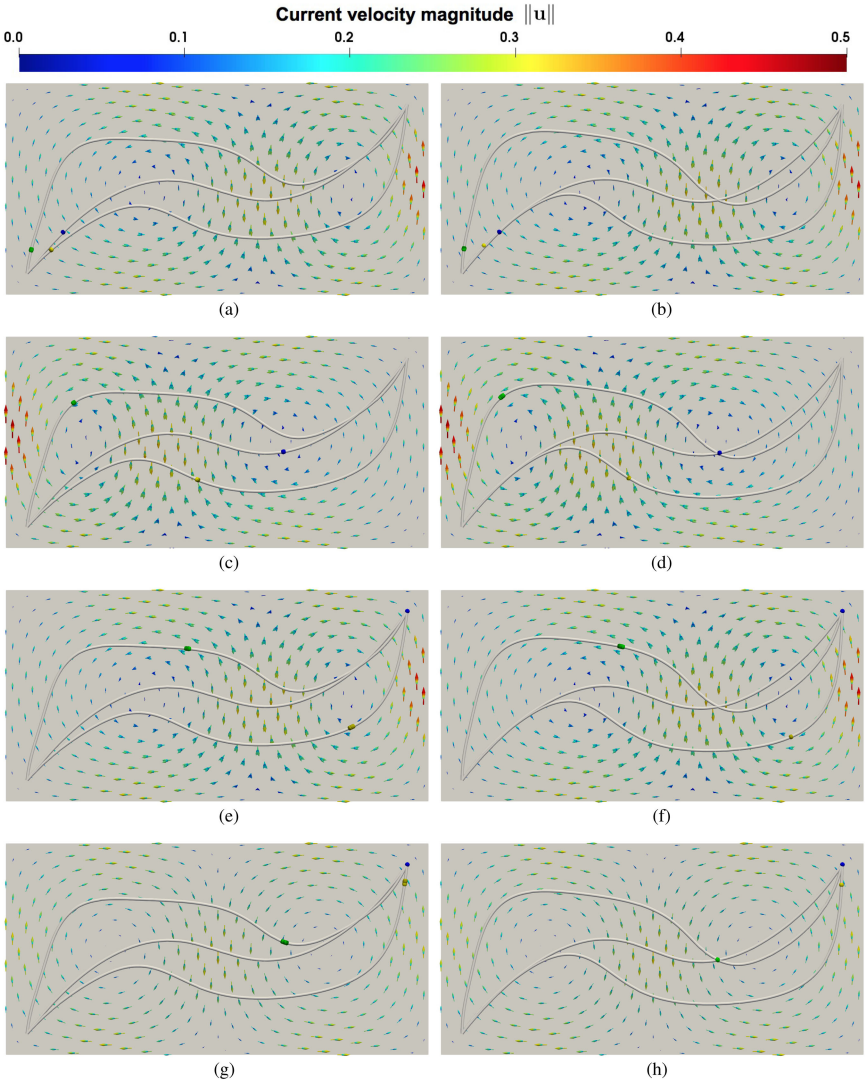

Fig. 15. Case 2. Optimal paths (lines) and distributions of the AUV position (spheres) at given selected times, obtained from the solution of the MEP. The arrows represent the local velocity vectors of the flow field ensemble. The blue spheres (●) indicate the solution with $T^{\text{fixed}} = 80$, the yellow spheres (●) with $T^{\text{fixed}} = 125$, and the green spheres (●) with $T^{\text{fixed}} = 170$. (a) $\beta = 0$ (risk averse), snapshot at time 10. (b) $\beta = 1$ (risk neutral), snapshot at time 10. (c) $\beta = 0$ (risk averse), snapshot at time 52. (d) $\beta = 1$ (risk neutral), snapshot at time 52. (e) $\beta = 0$ (risk averse), snapshot at time 90. (f) $\beta = 1$ (risk neutral), snapshot at time 90. (g) $\beta = 0$ (risk averse), snapshot at time 120. (h) $\beta = 1$ (risk neutral), snapshot at time 120.

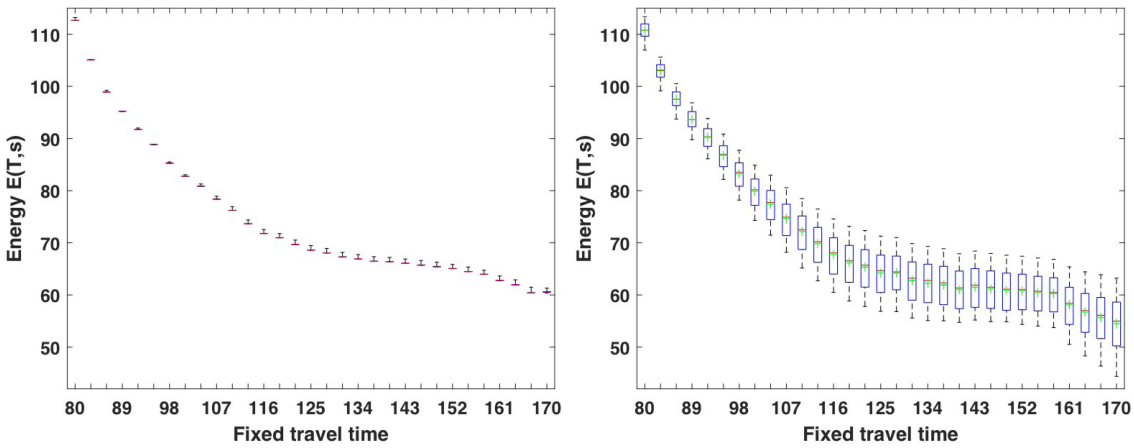

Fig. 16. Case 2. Time–energy Pareto-optimal curve with box-plot for the distribution of $E(s)\,\forall s \in \mathcal{S}$. In each box, the central red mark indicates the median, the green (+) indicates the mean, and the bottom and top edges of the box indicate the 25th and 75th percentiles of the distribution of energy spent, respectively. (a) $\beta = 0$ (risk averse). (b) $\beta = 1$ (risk neutral).

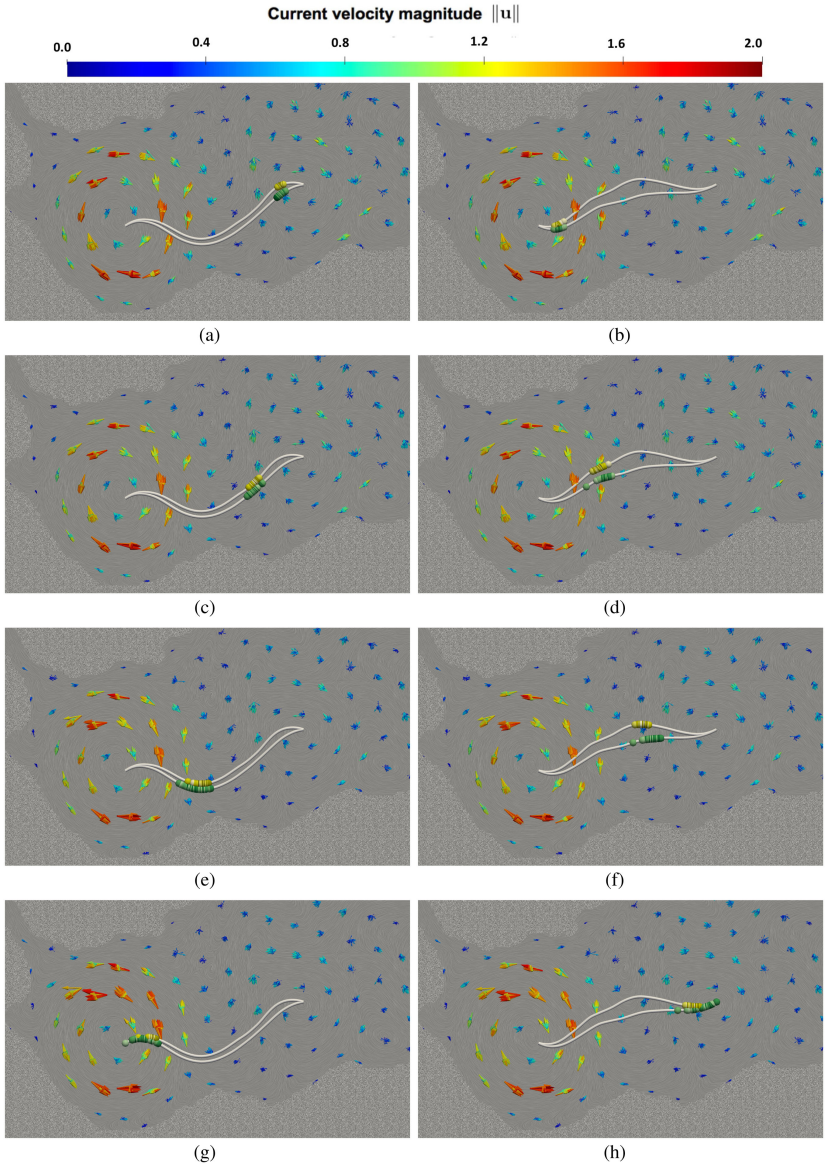

Fig. 17. Case 3. Optimal paths (gray lines) and distributions of the AUV position (spheres) obtained from the solutions of the MTP. The arrows represent the local velocity vectors of the flow field ensemble. The green spheres (●) indicate the solution with $\beta = 1$ (risk neutral) and the yellow spheres (●) indicate the solution with $\beta = 0$ (risk averse). (a) Instance I, snapshot at time 6 h. (b) Instance II, snapshot at time 6 h. (c) Instance I, snapshot at time 12 h. (d) Instance II, snapshot at time 12 h. (e) Instance I, snapshot at time 24 h. (f) Instance II, snapshot at time 24 h. (g) Instance I, snapshot at time 36 h. (h) Instance II, snapshot at time 33 h.

obtained for three fixed travel times are distinct; see Fig. 15. However, the solution paths for those fixed times obtained with $\beta = 0$ and $\beta = 1$ are similar, as can be seen by comparing the right and left sides of Fig. 15. In contrast to Case 1, there is no region of the domain with uniform low currents. Therefore, with increasing travel times, the solution paths change and have to adapt to the flow. Note that the distribution of the positions is almost collapsed to a single sphere, which does not represent a similar behavior in the distribution of energy consumption for each grid point.

Fig. 16(a) and (b) illustrates the time–energy Pareto curves with box-plots for $\beta = 0$ and $\beta = 1$, respectively. Both curves monotonically decrease as we increase the (selected) travel time.

In these figures, we can observe that the distribution of the energy consumption for $\beta = 0$ is almost collapsed to a single value, whereas the range of the distribution for $\beta = 1$ is larger and increases with the (selected) travel time.

The solutions for $\beta = 0$ represent robust solutions because there is small variation of the energy consumption for the entire range of travel times considered. For example, for $T^{\text{fixed}} = 170$, compare the distribution of the energy consumption with $\beta = 0$ and $\beta = 1$.

The range of the distribution of the energy consumption increases with travel time for $\beta = 1$; see Fig. 16(b). This increase indicates that as the (selected) travel time increases, the impact of the uncertainty on the energy consumption is higher. The space domain does not exhibit regions with uniform low current, but rather a stochastic transient double-gyre flow; therefore, as the travel time increases, the vehicle is always subject to the variability of the flow. Thus, for the larger

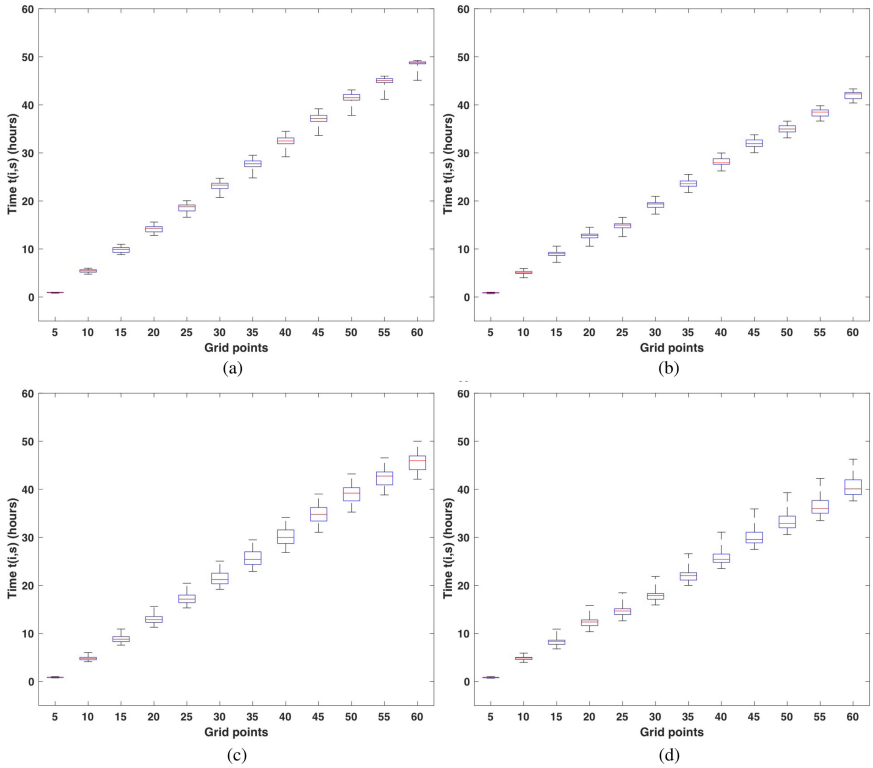

Fig. 18. Case 3. Box-plot of the distribution of times $t(i, s)\ \forall s \in \mathcal{S}$, for selected grid points i, obtained from the solution of the MTP. In each box, the central red mark indicates the median, and the bottom and top edges indicate the 25th and 75th percentiles of the travel time distribution, respectively. (a) Instance I, $\beta = 0$ (risk averse). (b) Instance II, $\beta = 0$ (risk averse). (c) Instance I, $\beta = 1$ (risk neutral). (d) Instance II, $\beta = 1$ (risk neutral).

travel times, the vehicle is exposed to a wider distribution of currents.

C. Case 3

In this case, we consider realistic flow fields described by an ensemble generated using an assimilative OGCM in the Red Sea. The objective is to demonstrate the capabilities of the proposed models and optimization approach to handling realistic multiple flow fields in a single problem, as an extension of previous work [32]. Even though the navigation is 3-D time-dependent inherently, we address a surface-navigation using the MTP. This focus enables visualizing trajectories, AUV positions, and a straight forward analysis of the predicted results. As mentioned before, two instances are considered. In Instance I, the vehicle starts in a region of relatively low current and heads toward the center of a strong vortex. In Instance II, the reverse situation occurs as the starting point and destination are switched. Note that due to the time-varying uncertain current field, the distribution of the current fields differs at common path locations in Instances I and II. For example, the AUV does not cross the left vortex at the same time, and thus, the AUV experiences different currents.

Fig. 17 shows the two paths obtained for $\beta = 1$ (risk neutral) and $\beta = 0$ (risk averse) with the MTP, for both instances. We observe that in regions of weak currents, the paths tend to be straight lines, whereas in strong currents or regions of strong shear, the AUV path exhibits appreciable curvature, which illustrates the impact of currents.

In Instance I (left column in Fig. 17), the path starts oriented toward the South West with an inflection point below the destination, namely to take advantage of the vortex's strong current field as the AUV approaches its destination. In contrast, in Instance II, the starting point is below the destination, and therefore, the path takes advantage of the vortex field to move up, heading to the destination point.

Comparing the risk-neutral and risk-averse paths, one observes a smaller difference between them in Instance I, and a larger difference in Instance II; compare the left and columns in Fig. 17. This deviation constitutes a solution of the risk-averse path to minimize the 10% ($\beta = 0$ and $\alpha = 0.90$) largest travel times. In Instance II, the starting point in the vortex center does not provide flexibility to the path to adapt to the strong flow, as in Instance I. Therefore, the vortex induces a larger deviation between paths due to the impact of the strongest currents.

The distribution of travel times at each grid point and the final travel times are presented in Fig. 18. We observe that Instance II has shorter expected travel times for both the risk-neutral and risk-averse solutions than Instance I. However, the difference is not significant, reflecting the optimization framework adapting to the uncertain flow and choosing alternative paths that minimize travel time. Similar patterns in the distribution of travel times along the path are obtained with risk-neutral and risk-averse results.

VI. Conclusion

We proposed an ensemble-based approach to plan the path of an AUV operating in transient and uncertain current fields. For this purpose, we developed a robust, multiobjective, and risk-aware framework. This optimization framework is based on a stochastic programming methodology incorporating a risk-aware objective function that accounts for the variability of the ensemble, and accommodating solutions that may not necessarily coincide with a deterministic solution corresponding to a specific member of the ensemble. The stochastic problems are used to minimize a risk measure of the total travel time or energy expenditure. We relied on an objective function that integrates a risk-neutral (defined by the expectation operator), and risk-averse (defined by the CVaR) measures. We use the CVaR of the total travel time to measure the risk of long travel times, and the CVaR of energy consumption to measure high energy expenditures. We compared the stochastic solution with the deterministic solution using the VSS measure, and estimated the EVPI to assess the value of perfect flow field forecasts.

We tested the proposed framework using two synthetic cases and a real application in the Gulf of Aden. In the two synthetic cases, the MTP results show that there is a significant difference between the optimal paths from the stochastic solutions and the EV solution, and with the solution of the MTP considering only one element of the ensemble per problem. For the MEP case, as the travel time increases from its minimum value, the energy spent monotonically decreases. As in the MTP case, the solutions of the risk-neutral measure have a wider distribution in the energy consumption than those obtained with the risk-averse measure. In the first case, the paths have the same shape for different arrival times but differ in depth; however, in the second case, because of the unsteadiness of the current field, the paths have different shapes for different arrival times. The box-plot Pareto curves show that in the first case, the distribution of the energy consumption gets narrower as the arrival time increases; however, in the second case, they get wider. This occurs because in the first case, the AUV can avoid a strong current by navigating at lower depth, whereas this is not possible in the second case. We also demonstrated the application of the proposed approach through experiments with a realistic OGCM ensemble. In particular, results obtained for the MTP revealed appreciable differences between the paths corresponding to risk-neutral and risk-averse solutions. As in the synthetic cases, the solutions of the risk-neutral measure exhibited a wider distribution in the arrival time than those of the risk-averse measure. Finally, detailed visualizations were used to examine the predicted box-plot Pareto-optimal solutions. These visualizations illustrate how the vehicle's path adapts to the structure of the uncertain current field, as well as its unsteadiness, to minimize total travel time and energy consumption.

The work will evolve in two directions in the future. First, we plan to incorporate a sample average approximation approach to study the impact of the sample size on the solution paths, travel times, and energy consumption. This approach will also enable the calculation of estimators and confidence intervals of the expected travel time and CVaR of the travel time for a solution path. The second direction will consider the inclusion of other sources of uncertainty, e.g., related to localization of the AUV, as well as more general forms of the objective function, namely to reflect mission specific goals.

References

[1] H. Stommel, "The Slocum mission," *Oceanography*, vol. 2, pp. 22–25, 1989.

[2] D. R. Blidberg, R. M. Turner, and S. G. Chappell, "Autonomous underwater vehicles: Current activities and research opportunities," *Robot. Auton. Syst.*, vol. 7, no. 2, pp. 139–150, 1991.

[3] M. P. Aghababa, "3D path planning for underwater vehicles using five evolutionary optimization algorithms avoiding static and energetic obstacles," *Appl. Ocean. Res.*, vol. 38, pp. 48–62, 2012.

[4] J. Yuh, "Design and control of autonomous underwater robots: A survey," *Auton. Robots*, vol. 8, no. 1, pp. 7–24, 2000.

[5] M. Soulignac, P. Taillibert, and M. Rueher, "Adapting the wavefront expansion in presence of strong currents," in *Proc. IEEE Robot. Automat. Int. Conf.*, 2008, pp. 1352–1358.

[6] T. Lolla, M. P. Ueckermann, K. Yigit, P. J. Haley, and P. F. J. Lermusiaux, "Path planning in time dependent flow fields using level set methods," in *Proc. IEEE Int. Conf. Robot. Automat.*, 2012, pp. 166–173.

[7] Y. K. Hwang and N. Ahuja, "Gross motion planning—A survey," *ACM Comput. Surv.*, vol. 24, no. 3, pp. 219–291, Sep. 1992.

[8] M. Chyba, T. Haberkorn, R. Smith, and S. Choi, "Design and implementation of time efficient trajectories for autonomous underwater vehicles," *Ocean Eng.*, vol. 35, no. 1, pp. 63–76, 2008.

[9] Z. Zeng, A. Lammas, K. Sammut, F. He, and Y. Tang, "Shell space decomposition based path planning for AUVs operating in a variable environment," *Ocean Eng.*, vol. 91, pp. 181–195, 2014.

[10] S. El Mohtar, I. Hoteit, O. Knio, L. Issa, and I. Lakkis, "Lagrangian tracking in stochastic fields with application to an ensemble of velocity fields in the red sea," *Ocean Model.*, vol. 1–31, pp. 1–14, 2018.

[11] I. Hoteit, X. Luo, M. Bocquet, A. Kohl, and B. Ait-El-Fquih, "Data assimilation in oceanography: Current status and new directions," in *New Frontiers in Operational Oceanography*, E. P. Chassignet, A. Pascual, J. Tintore, and J. Verron, Eds. GODAE Ocean View, Aug. 2018, p. 815.

[12] Z. Zeng, L. Lian, K. Sammut, F. He, Y. Tang, and A. Lammas, "A survey on path planning for persistent autonomy of autonomous underwater vehicles," *Ocean Eng.*, vol. 110, no. A, pp. 303–313, 2015.

[13] J. A. Sethian, *Level Set Methods and Fast Marching Methods: Evolving Interfaces in Computational Geometry, Fluid Mechanics, Computer Vision, and Materials Science*. Cambridge, U.K.: Cambridge Univ. Press, 1999, vol. 3.

[14] J. J. Kuffner and S. M. LaValle, "RRT-connect: An efficient approach to single-query path planning," in *Proc. IEEE Int. Conf. Robot. Automat. Symp.*, vol. 2, 2000, pp. 995–1001.

[15] O. Khatib, "Real-time obstacle avoidance for manipulators and mobile robots," in *Autonomous Robot Vehicles*, I. J. Cox and G. T. Wilfong, Eds. New York, NY, USA: Springer, 1990, pp. 396–404.

[16] M. Mitchell, *An Introduction to Genetic Algorithms*. Cambridge, MA, USA: MIT Press, 1996.

[17] A. Alvarez, A. Caiti, and R. Onken, "Evolutionary path planning for autonomous underwater vehicles in a variable ocean," *IEEE J. Ocean. Eng.*, vol. 29, no. 2, pp. 418–429, Apr. 2004.

[18] T. Schouwenaars, B. D. Moor, E. Feron, and J. How, "Mixed integer programming for multi-vehicle path planning," in *Proc. Eur. Control Conf.*, 2001, pp. 2603–2608.

[19] N. K. Yilmaz, C. Evangelinos, P. F. J. Lermusiaux, and N. M. Patrikalakis, "Path planning of autonomous underwater vehicles for adaptive sampling using mixed integer linear programming," *IEEE J. Ocean. Eng.*, vol. 33, no. 4, pp. 522–537, Oct. 2008.

[20] T. Wang, R. M. Lima, L. Giraldi, and O. M. Knio, "Trajectory planning for autonomous underwater vehicles in the presence of obstacles and a nonlinear flow field using mixed integer nonlinear programming," *Comput. Oper. Res.*, vol. 101, pp. 55–75, 2019.

[21] S. Albarakati, R. M. Lima, L. Giraldi, I. Hoteit, and O. Knio, "Optimal 3D trajectory planning for AUVs using ocean general circulation models," *Ocean Eng.*, vol. 188, 2019, Art. no. 106266.

[22] O. Souissi, R. Benatitallah, D. Duvivier, A. Artiba, N. Belanger, and P. Feyzeau, "Path planning: A 2013 survey," in *Proc. Int. Conf. Ind. Eng. Syst. Manage.*, 2013, pp. 1–8.

[23] A. A. Pereira and G. S. Suhatme, "Minimum-risk time-expanded planning for AUVs using ocean current predictions," *J. Field Robot.*, vol. 30, no. 5, pp. 741–762, 2013.
[24] A. A. Pereira, J. Binney, G. A. Hollinger, and G. S. Sukhatme, "Risk-aware path planning for autonomous underwater vehicles using predictive ocean models," *J. Field Robot.*, vol. 30, no. 5, pp. 741–762, 2013.
[25] D. Kularatne, H. Hajieghrary, and M. A. Hsieh, "Optimal path planning in time-varying flows with forecasting uncertainties," in *Proc. IEEE Int. Conf. Robot. Automat.*, 2018, pp. 4857–4864.
[26] D. N. Subramani, Q. J. Wei, and P. F. Lermusiaux, "Stochastic time-optimal path-planning in uncertain, strong, and dynamic flows," *Comput. Methods Appl. Mech. Eng.*, vol. 333, pp. 218–237, 2018.
[27] D. N. Subramani and P. F. Lermusiaux, "Risk-optimal path planning in stochastic dynamic environments," *Comput. Methods Appl. Mech. Eng.*, vol. 353, pp. 391–415, 2019.
[28] T. Wang, O. P. Le Maître, I. Hoteit, and O. M. Knio, "Path planning in uncertain flow fields using ensemble method," *Ocean Dyn.*, vol. 66, no. 10, pp. 1231–1251, 2016.
[29] R. T. Rockafellar and S. Uryasev, "Optimization of conditional value-at-risk," *J. Risk*, vol. 2, pp. 21–41, 2000.
[30] J. R. Birge and F. Louveaux, *Introduction to Stochastic Programming*. Berlin, Germany: Springer, 2011.
[31] C.-L. Hwang and A. S. M. Masud, *Multiple Objective Decision Making—Methods and Applications: A State-of-the-Art Survey*. Berlin, Germany: Springer, 1979.
[32] S. Albarakati, R. M. Lima, T. Theußl, I. Hoteit, and O. Knio, "Optimal 3D time-energy trajectory planning for AUVs using ocean general circulation models," *Ocean Eng.*, vol. 218, 2020, Art. no. 108057.
[33] S. C. Shadden, F. Lekien, and J. E. Marsden, "Definition and properties of Lagrangian coherent structures from finite-time Lyapunov exponents in two-dimensional aperiodic flows," *Physica D, Nonlinear Phenomena*, vol. 212, no. 3, pp. 271–304, 2005.
[34] H. Toye *et al.*, "Ensemble data assimilation in the Red Sea: Sensitivity to ensemble selection and atmospheric forcing," *Ocean Dyn.*, vol. 67, no. 7, pp. 915–933, 2017.
[35] H. Toye, S. Kortas, P. Zhan, and I. Hoteit, "A fault-tolerant HPC scheduler extension for large and operational ensemble data assimilation: Application to the Red Sea," *J. Comput. Sci.*, vol. 27, pp. 46–56, 2018.
[36] I. Hoteit *et al.*, "A MITgcm/DART ensemble analysis and prediction system with application to the Gulf of Mexico," *Dyn. Atmos. Oceans*, vol. 63, pp. 1–23, 2013.
[37] F. Yao *et al.*, "Seasonal overturning circulation in the Red Sea: Part 1. Model validation and summer circulation," *J. Geophys. Res., Oceans*, vol. 119, pp. 2238–2262, 2014.
[38] F. Yao *et al.*, "Seasonal overturning circulation in the Red Sea: Part 2. Winter circulation," *J. Geophys. Res., Oceans*, vol. 119, pp. 2263–2289, 2014.
[39] GAMS, General Algebraic Modeling System (GAMS) Release 25.1.2, Washington, DC, USA, 2018.
[40] A. Wächter and L. T. Biegler, "On the implementation of an interior-point filter line-search algorithm for large-scale nonlinear programming," *Math. Program.*, vol. 106, no. 1, pp. 25–57, 2006.

Sultan Albarakati received the Ph.D. degree in applied mathematics and computational sciences from the King Abdullah University of Science and Technology, Thuwal, Saudi Arabia, in 2020.

His research interests include mathematical programming, optimization under uncertainty, and optimal path planning of autonomous underwater vehicles.

Ricardo M. Lima received the Ph.D. degree in chemical engineering from the Faculty of Engineering, University of Porto, Porto, Portugal, in 2006.

He was a Postdoc Fellow and a Researcher with the Department of Chemical Engineering, Carnegie Mellon University, Pittsburgh, PA, USA, from 2006 to 2011, and an invited Researcher with PPG Industries from 2008 to 2011. He was a Marie Curie Fellow with the National Laboratory of Energy and Geology, Lisbon, Portugal, from 2011 to 2014. Since 2014, he has been a Research Scientist with the King Abdullah University of Science and Technology, Thuwal, Saudi Arabia. His research interests include mathematical programming, energy systems, and optimal path planning of autonomous underwater vehicles.

Thomas Theußl received the master's degree in computer science from the Vienna University of Technology, Vienna, Austria, in 2000.

He is currently a Visualization Scientist with Visualization Core Lab, King Abdullah University of Science and Technology, Thuwal, Saudi Arabia.

Ibrahim Hoteit received the M.S. and Ph.D. degrees in applied mathematics from the University of Joseph Fourier, Grenoble, France, in 1998 and 2002, respectively.

He is currently a Professor in the earth sciences and engineering program with the King Abdullah University of Science and Technology (KAUST), Thuwal, Saudi Arabia. He is the Lead of the Virtual Red Sea Initiative, a joint initiative with the Scripps Institution of Oceanography, MIT, and Plymouth Marine Laboratory. He is also the Associate Director of the Saudi Aramco Marine Environment Research Center, KAUST. He has coauthored more than 190 papers. His research interests include the modeling of oceanic and atmospheric systems on supercomputers and the analysis of their circulation and variability, with specific interest in data assimilation and inverse problems and associated uncertainty quantification for large-scale systems.

Dr. Hoteit is a corecipient of five best conference paper awards. He is an Associate Editor for *PLoS ONE*, *Computational Geosciences*, *Mathematics of Climate and Weather Forecasting*, and *Atmospheric Science Letters*, and is a member of the American and European Geophysical Unions, the Society of Industrial and Applied Mathematics, and an elected member of the UNESCO Center of Pure and Applied Mathematics.

Omar Knio received the Ph.D. degree in mechanical engineering from the Massachusetts Institute of Technology (MIT), Cambridge, MA, USA, in 1990.

He held a Postdoctoral Associate position at MIT, before joining the Mechanical Engineering Faculty, Johns Hopkins University, Baltimore, MD, USA, in 1991. In 2011, he joined the Mechanical Engineering and Materials Science Department, Duke University, Durham, NC, USA, where he was an Associate Director of the Center for Material Genomics. In 2012, he was named the Edmund T. Pratt, Jr., Professor of Mechanical Engineering and Materials Science at Duke. In 2013, he joined AMCS Program at KAUST, where he was the Deputy Director of the SRI Center for Uncertainty Quantification in Computational Science and Engineering.

Dr. Knio is the recipient of an Associated Western Universities Faculty Fellowship Award in 1996, a Friedrich Wilhelm Bessel Award in 2003, an R&D100 Award in 2005, and a Distinguished Alumnus Award from the American University of Beirut in 2005.